Journal of Materials Chemistry A

Scalable Open-Air Deposition of Compact ETL TiO_x on Perovskite for Fullerene-Free Solar Cells

Journal:	*Journal of Materials Chemistry A*
Manuscript ID	TA-ART-09-2020-008554.R1
Article Type:	Paper
Date Submitted by the Author:	15-Oct-2020
Complete List of Authors:	Chen, Justin; Stanford University, Materials Science and Engineering Hilt, Florian; Stanford University, Materials Science and Engineering Rolston, Nicholas; Stanford University, Applied Physics Dauskardt, Reinhold; Stanford University, Materials Science and Engineering

SCHOLARONE™
Manuscripts

Scalable Open-Air Deposition of Compact ETL TiO_x on Perovskite for Fullerene-Free Solar Cells

Justin P. Chen,[a,†] Florian Hilt,[a,c,†] Nicholas Rolston,[b] Reinhold H. Dauskardt[a]*

[a] Department of Materials Science and Engineering

Stanford University, Stanford, CA, 94305-2205, United States

E-mail: rhd@stanford.edu

[b] Department of Applied Physics

Stanford University, Stanford, CA, 94305-2205, United States

[c] Now at Institut Photovoltaïque d'Île-de-France (IPVF), 91120 Palaiseau, France

† Equal Contribution

Keywords: Electron Transport Layer, Stability, Titanium Oxide, Perovskite Solar Cells, Chemical Vapor Deposition

Abstract

We report on a scalable, low-temperature TiO_x electron transport layer (ETL) produced directly on top of perovskite in an inverted architecture device by an open-air chemical vapor deposition (OA-CVD) process. The OA-CVD pyrolysis of a titanium ethoxide precursor forms a fully inorganic, conformal, and compact TiO_x film. The resultant film is mechanically robust and exhibits a fracture toughness 30-fold higher than commonly used fullerene-based ETL films. The TiO_x is an effective barrier layer against environmental degradation—unencapsulated devices with the TiO_x ETL retain 60% of their initial efficiency after 1000 hours in ambient aging conditions—compared to devices with a fullerene ETL which were inoperable after 144 hours. Inverted architecture devices with an optimized TiO_x ETL thickness of 70nm exhibited high open-circuit voltages of 1.08V. We comment on the photocatalytic properties of TiO_x and the influence of an amorphous film on maximum power point stability.

Introduction

Since the development of the first perovskite solar cell (PSC),[1] significant progress has been made in the design of devices to optimize their optoelectronic performances to reach power conversion efficiencies of 25%, comparable to the performance of silicon solar cells.[2] Fullerene-based, organic electron transport layers (ETLs), such as [6,6]-phenyl C_{61} butyric acid methyl ester (PCBM), C_{60}, and their derivatives have been used extensively and are by far the most common ETLs deposited on the perovskite for the inverted, P-I-N architecture due to their low-temperature processing.[3–7] However, the high cost of organic precursors[8] and their typical deposition methods of spin-coating and vacuum thermal evaporation limit large-scale adoption. More importantly, the susceptibility of these materials to environmental degradation leads to PSCs with poor chemical and mechanical stability and limited lifetimes.[9,10] Previous work from our lab showed that the measured fracture resistances, G_c – a key metric for thermomechanical reliability – of fullerene-based charge transport layers were so low ($G_c < 0.2$ J/m²) that they significantly limit the commercialization potential of this architecture as a viable technology.[11–13]

Inorganic charge transport layers have demonstrated better barrier functionality against environmental species as liquid water-resistant devices that are more stable to humidity.[14] Their improved thermal stability allows them to double as buffer layers enabling sputtered transparent conducting oxides[15] for tandem applications and compatibility with high-temperature encapsulation methods in industry-standard lamination processes.[16] Despite their advantages, inorganic charge transport layers have not been readily adopted as the sole charge transport layer, especially on top of perovskite in inverted P-I-N architectures because processing methods that involve high energy particle bombardment or high temperature annealing or sintering steps also damage the perovskite layer. Previous reports of inorganic ETLs for inverted devices typically incorporate an intermediary fullerene-based layer,[14,17–19] while a limited number of studies on fullerene-free inverted devices rely on spin-coating of sol-

gels[20–22] or vacuum-based depositions[23] neither of which are amenable to large scale or in-line production.

A dense TiO_2 layer can be prepared by a variety methods such as spin coating, sol-gel,[24] aerosol spray pyrolysis,[25–27] atomic layer deposition,[28,29] magnetron sputtering,[30–32] chemical vapor deposition,[33] or electrochemical deposition.[34] However, these methods involve complicated fabrication procedures or equipment which need vacuum environments that dramatically increase the overall cost of fabrication or are less suitable for large area devices. In addition, solution-based film processing techniques for ETLs beneath the perovskite in N-I-P architecture are not typically transferrable for deposition on top of bare perovskite, which can easily be degraded by chemical solvents or under sintering conditions that are typical for producing compact TiO_2 films.

In this work, we use a scalable Open-Air Chemical Vapor Deposition (OA-CVD) process capable of depositing a compact TiO_x thin film directly on top of perovskite with inherent barrier properties as an effective n-type ETL for perovskite solar cells. It is an attractive low-energy and low-temperature alternative involving simple equipment that can be adopted for roll-to-roll and sheet-to-sheet processing, compatible with industrial manufacturing. The OA-CVD TiO_x deposited films have 30-fold higher fracture energy resistance than common organic ETL films, with more than 7-fold longer operational lifetimes when aged in ambient conditions.

Results and discussion

Open Air Chemical Vapor Deposition (OA-CVD)

A 250 nm thick TiO_x film was deposited with the OA-CVD experimental setup (**Figure 1a**) using a titanium ethoxide precursor in a nitrogen carrier gas with the deposition parameters listed in **Table S1**. Deposition parameters were carefully tuned to control the resultant film thickness. Top down scanning electron microscopy (SEM) images revealed densely packed ~50 nm in dia. grains comprised of ~5 nm dia. densely packed particles (**Figure 1b)**. SEM cross-sections (**Figure 1c**) revealed that the columnar grain morphology was dense and

compact without pinholes. The observed morphology was in contrast with a powder-like morphology that would be observed with powder aggregation initiating in the gas phase. The flash-evaporated titanium ethoxide precursor undergoes a thermal decomposition to cleave the hydrocarbon ligands similar to a process studied using *in-situ* mass spectroscopy with a comparable metal alkoxide of titanium isopropoxide.[35] The titanium ethoxide precursor with a lower boiling point (<250°C at 1 atm) was thus chosen over more common materials such as titanium isopropoxide or titanium butoxide (tetrabutyl titanate) (~315°C at 1 atm) because it is a liquid metal alkoxide with the fewest carbon bonds for undesired and extraneous cleavage sites beyond C-O bonds. Despite the high reactivity of metal alkoxide precursors with ambient moisture, the small nozzle-to-substrate distance (1mm) and hot exiting precursor vapors (≈100°C) limit nucleation to the substrate surface.

X-ray photoelectron spectroscopy (XPS) measurements of the OA-CVD deposited TiO_x film revealed primarily a 1:1.94 ratio of Ti to O species (**Figure S1**). There was negligible presence of a C_{1s} peak at 290eV binding energy, suggesting a more complete pyrolysis and vaporization of organic ligands possibly due to fewer methyl groups in titanium ethoxide, in contrast to previously reported results.[35] Due to the low-temperature deposition and anneal, the deposited TiO_x film was amorphous, as confirmed by Grazing Incidence X-Ray Diffraction (GIXRD) measurements (**Figure S2**).

TiO_x Film on Top of Perovskite

The morphology of OA-CVD deposited TiO_x films on top of a double cation perovskite layer with composition $Cs_{.17}FA_{.83}Pb(I_{.83}Br_{.17})_3$ (CsFA) were characterized using Atomic Force Microscopy (AFM) (**Figure 2**). Similar TiO_x films deposited on a silicon substrate were fabricated for comparison. The root-mean square surface roughness, R_q, of films were measured over a 1μm^2 area. The 30 nm and 100 nm thick TiO_x films deposited on silicon exhibited low RMS roughness < 5 nm. This suggests that the higher RMS roughness of TiO_x on perovskite (> 10 nm) is a result of the TiO_x layer conforming to the inherent rougher morphology of the underlying perovskite with RMS roughness > 15 nm. Indeed, the AFM scan

images of TiO_x on perovskite have visibly darker and deeper valleys than the scan images of TiO_x on silicon.

The bare perovskite is exposed to chemical vapors during OA-CVD film deposition, and it is imperative that formation of the ETL simultaneously preserves the fragile perovskite structure. XRD (2θ-ω) measurements were performed on a glass/perovskite test architecture before and after TiO_x film deposition (**Figure 3a**), where the main perovskite (001) peak at $2\theta = 14°$ is unchanged. A small peak at $2\theta = 12.75°$ attributed to PbI_2 (001) increases slightly in perovskite/TiO_x films, but additional (002) and (003) reflections from PbI_2 are not observed. The spectra indicate that the OA-CVD process does not significantly damage or alter the perovskite crystal structure. UV-Vis spectroscopy measurements before and after TiO_x film deposition also confirm that the optical absorption of the perovskite layer remains unchanged (**Figure 3b**).

Device Performance and Optoelectronic Properties

The TiO_x ETL was integrated into an inverted P-I-N device architecture (ITO/NiO_x/CsFA perovskite/TiO_x/Al) and cross-sectionally imaged in **Figure 4a**. The energy band diagram of the entire device is illustrated in **Figure S3**. During fabrication and testing of the PSCs, we discovered that appropriate selection of the top metal electrode was crucial in achieving high J_{sc} values. Current-voltage measurements of a glass/ITO/TiO_x/electrode test structure showed significantly higher resistance with an Ag top electrode compared to an Al electrode (**Figure S4**). Ti and Au contacts on top of TiO_x also yielded similarly low J_{sc} values. Several reports in literature of metal contacts above a bare TiO_x film were also limited to using an Al top electrode, possibly due to its lower work function allowing an ohmic contact with TiO_x.[14,18,19]

Based on the experimental setup of OA-CVD illustrated in **Figure 1a** and as mentioned previously, the TiO_x thickness is readily tunable. **Figure 4b** plots the current density-voltage (J-V) curves of several champion devices with TiO_x thicknesses of 30, 70, 100, and 150 nm. The optimal thickness at 70 nm yielded devices that were 13.3% efficient with an open-circuit voltage (V_{oc}) of 1.08V, short-circuit current density (J_{sc}) of 19.8 $mA{\cdot}cm^{-2}$, and fill factor (FF) of

62.4% on an active area of 0.21 cm^2. The lower J_{sc} and FF but higher V_{oc} of devices (**Table S2**) was attributed to the presence of PbI_2 at the perovskite/TiO_x interface as evidenced by the PbI_2 peak in **Figure 3a** after TiO_x deposition. The PbI_2 peak increased in intensity at the thickest TiO_x film because the significantly longer processing time subjected the perovskite layer to more thermal degradation (**Figure S5**). Increasing the TiO_x thickness resulted in poorer device performance due to decreases in J_{sc} from more series resistance (**Figure S6**) and decreases in V_{oc}. In contrast, thinner TiO_x films led to poor device performance since the rougher perovskite layer **(Figure 2**) was not fully planarized and resulted in incomplete coverage of the perovskite surface with visible metal-halide induced degradation after deposition.[36]

The optoelectronic charge transfer properties of the OA-CVD deposited TiO_x film were compared with those of C_{60}/BCP, an organic ETL combination used in inverted P-I-N devices as reported by others.[37–40] Glass/perovskite/ETL test structures characterized with steady-state photoluminescence showed quenching at an emission wavelength of 750 nm (**Figure 4c**), closely matching the expected band gap of 1.63 eV for the CsFA composition[41] used in this study. Time-resolved photoluminescence (TRPL) measurements on these structures (**Figure 4d**) revealed short TRPL lifetimes for C_{60}/BCP (τ = 13 ns) indicating fast charge quenching and charge transfer. The TRPL lifetimes for TiO_x (τ = 36 ns), albeit longer than those of C_{60}/BCP, are within the range reported by others[42] and indicate that TiO_x ETLs can effectively extract photogenerated electrons resulting in high V_{oc} values.

Device Operational Stability

Steady-state device performance was characterized with unencapsulated TiO_x ETL devices with maximum-power point tracking (MPPT) under full spectrum illumination in ambient conditions (45% RH, 25°C). The normalized efficiency of the TiO_x ETL device decreased to 60% of its initial value after 600 seconds of MPPT (**Figure 5a**). Devices were able to recover their initial efficiency in single J-V scans post-MPPT measurement. The transient instability behavior in TiO_x ETL devices is likely related to device hysteresis effects (**Figure S7**) during repeated MPPT perturb-and-measure steps. Hysteretic effects are less

evident in C_{60}/BCP ETL devices (**Figure S8**) which benefit from the shorter observed TRPL lifetimes (**Figure 4d**). In addition to ion migration in the perovskite layer, several authors report that hysteresis may stem from inefficient charge extraction at the perovskite/charge transport layer interface, leading to a capacitive current.[43–45] Thermal annealing is a simple method that can improve a transport layer's charge extraction efficiency and electronic properties through crystallization of amorphous domains and passivation of defects leading to reduced non-radiative recombination of charge carriers. An OA-CVD deposited TiO_x film annealed in ambient at 450°C for 30 minutes produced a film with anatase crystal phases (**Figure S2**) and a resistivity almost two orders of magnitude lower than the amorphous film (**Table S3**).

Since the thermal sensitivity of perovskite restricts a high temperature anneal treatment of the amorphous TiO_x film on top of perovskite, two sets of devices were fabricated in a normal N-I-P architecture (FTO/TiO_x/ perovskite/spiro-OMeTAD/Ag), where the ETL was either a TiO_x film as deposited or post-thermally annealed as TiO_2. Devices with the annealed TiO_2 ETL demonstrated a stable power output (**Figure 5a**), suggesting that a more conductive transport layer with fewer defects may mitigate a decaying power output instability. More work is needed to understand the relationship between transport layer conductivity, defect-mediated non-radiative recombinations, and MPPT. Given that the thermal stability of perovskite does not allow high temperature annealing of inorganic ETLs, other reports of less-common inorganic ETL materials such as CeO_x[22] and Nb_2O_5[23,46] may be promising on top of perovskite due to their higher conductivities in the amorphous phase.

Despite MPPT stability challenges, P-I-N devices (ITO/NiO_x/perovskite/ETL/metal) with a TiO_x ETL demonstrated impressive barrier properties against environmental species when compared to an organic ETL combination of C_{60}/BCP. **Figure 5b** compares the normalized efficiencies of the two ETLs taken at select time points as the devices shelf-aged in uncovered and ambient conditions (45% RH, 25°C) for 1000 hours. Devices with C_{60}/BCP ETL were completely inoperable after 144 hours of aging. Devices with a TiO_x ETL initially experienced

a slight increase in efficiency, possibly due to air passivation of defects, and then remained operational past 1000 hours of aging.

TiO_x Material Stability and Mechanical Integrity

Although TiO_2 is a widely used ETL, it is also a known photocatalyst, and several reports have investigated the ultraviolet (UV) stability of TiO_2-based PSCs.[47–50] TiO_2 in the presence of UV light will catalyze the formation of radical species from oxygen or water in air, which can adversely react with and degrade the perovskite film. The UV stability of glass/perovskite/TiO_x test structures was characterized by comparing UV-Vis absorption spectra before and after aging under 1-sun illumination (through the glass side) for 24 hours in air (45% RH) at 40°C. **Figure 6a** highlights a dramatic change in the absorption spectra of the TiO_x test structures compared to the pristine test structure. In contrast, the absorption spectra change in bare perovskite or bare perovskite with other ETL materials was minimal under the same testing conditions (**Figure S9a-c**), suggesting that the TiO_x/perovskite interface is the likely cause for accelerated degradation of the perovskite layer. XRD measurements of the aged TiO_x test structure revealed the presence of many additional peaks, including those at $2\theta = 26.65°$ and 37.9°, corresponding to the (002) and (003) reflections of PbI_2, respectively (**Figure S10**).

To confirm the role of the photocatalytic effect, TiO_x test structures were subsequently aged in conditions either without light or without air species. The similar post absorption spectra in **Figure 6a** suggests that the combination of light and air must be present to observe the large spectra change associated with the accelerated photocatalytic degradation. This result indicates that the UV-based degradation can be mitigated through standard device encapsulation procedures. Interestingly, we also observed that test architectures of glass/TiO_x/perovskite—representative of more commonly used N-I-P configurations—exhibited minimal change in absorption post-aging in **Figure S9d**, possibly due to different interface chemistry for a perovskite layer deposited over the TiO_x film.

In addition to optoelectronic stability, the thermomechanical reliability of a solar cell is equally crucial. The use of a mechanically robust ETL will ensure that the device remains intact through the mechanical stresses from the fabrication processes and thermal cycling during standard operation. The cohesive fracture energy (G_c) of various ETLs were characterized by a Double Cantilever Beam (DCB) method in **Figure 6b**. OA-CVD deposited TiO_x films with an optimized thickness of 70nm yielded a G_c value of 6.1 $\pm$ 1.15 $J \cdot m^{-2}$, which is comparable to cohesive fracture energies reported for SiO_2.[51] These values are exceedingly higher (60x & 30x) than those of common fullerene-based ETL counterparts of PCBM and C_{60}, which have low cohesive fracture energies of 0.13 $\pm$ 0.05 $J \cdot m^{-2}$ and 0.22 $\pm$ 0.07 $J \cdot m^{-2}$, respectively. Indeed, the exceptionally fragile cohesive energies of these organic films altogether rule them out as viable technologies for scalable manufacturing and extended operation, and previous work has already observed delamination in the fullerene layer for fully encapsulated devices.[16]

Much of the focus in the perovskite field has been on achieving high efficiency devices by tuning the bottom transport and perovskite layers to optimize devices, with organic top layers that are easier to process without damaging the underlying perovskite layer. This work demonstrates a scalable technique for fabricating inorganic transport layers on top of perovskite. Future work should address improving device fill factor by examining how inorganic precursor choices (e.g. SnO_2,[52–57] CeO_x,[22] and Nb_2O_5[23,46]) and processing conditions can improve ETL conductivities and interfacial properties with the perovskite layer.

Conclusion

We have demonstrated PSCs with a fully inorganic ETL deposited on top of perovskite using open-air and scalable methods. The low-temperature OA-CVD method can deposit conformal and dense films with a controlled thickness while preserving the underlying perovskite structure. TiO_x ETL films demonstrate photoluminescence quenching, and inverted architecture devices with TiO_x exhibit high open-circuit voltages. Additionally, TiO_x ETL films are mechanically robust exhibiting improved barriers to moisture and air ingress than

competing organic ETLs. Future improvements to device performance and stability will focus on improving the interface between TiO_x and perovskite layers.

Experimental Methods

Open-Air Chemical Vapor Deposition of TiO_x

Titanium Ethoxide (CAS: 3087-36-3, Sigma Aldrich) was diluted with 20 vol.% toluene (anhydrous, DriSolv), and the precursor was stored in a glovebox when not in use. A flash evaporator provided by Plasmatreat GmbH (Hayward, CA, USA) was mounted on a gantry with a 1/8” pipe gas outlet nozzle set 1mm above the substrate surface. Substrates are placed on a hotplate at 100°C. Titanium oxide precursor is fed at 2μL/min along with 4 SLPM of carrier N_2 gas into the evaporator set at 250°C. The evaporator and gas exit nozzle are rastered over the surface of the substrate in a serpentine fashion with a path speed of 10cm/s and a line spacing of 0.5mm.

Perovskite Precursors

The perovskite precursor solution consisted of 285.5mg formamidinium iodide (FAI) (Dyseol), 88.3mg cesium iodide (CsI) (Sigma), 686.9mg lead iodide (PbI_2) (TCI), and 187.2mg of lead bromide (PbI_2) (TCI). All solvents were anhydrous and used as received (Acros). A 1.0M solution of $Cs_{.17}FA_{.83}Pb(I_{.83}Br_{.17})_3$ was made by dissolving the solid amounts above in 1.6mL of anhydrous *N,N*-Dimethylformamide (DMF) and 0.4mL Dimethylsulfoxide (DMSO) (4 :1 ratio) in a glovebox. The prepared perovskite solution was stirred at 60°C for 1 hr in inert atmosphere, then filtered with a 0.45 μm Durapore (PVDF) membrane filter. The solution was used within a month of mixing.

Device Fabrication

ITO-coated glass (Xin Yan, 10 Ω/□) was cleaned by successively sonicating in Extran detergent diluted 1:10 in DI water, pure DI water, acetone, and isopropanol for 10 minutes each before being treated in a UV-ozone chamber at 25 mW cm^{-2} for 15 min (Jelight Model 42). Then, 40 μL of NiO_x solution (291mg $NiNO_3$ hexahydrate in 940μL ethylene glycol and

60μL ethylene diamine all obtained from Sigma Aldrich) was spin-coated at 5000rpm for 30 seconds in air, then quickly placed on top a hot plate at 300°C for 1.5hr.

Perovskite films were spin-coated in a glovebox by first spreading 20μL of perovskite across the NiO_x film. The precursor was spun in a two-step program with the first step at 1000rpm for 12 seconds and the second step at 6000rpm for 30 seconds. During the last 5 seconds of the second step, 60μL of chlorobenzene (Sigma Aldrich) was quickly dispensed over the film. The substrates were then immediately placed on a hot plate at 100°C for 30min in the glovebox.

Devices with inorganic TiO_x ETLs were fabricated as described above. For the N-I-P structure, a spiro-OMeTAD solution was made by dissolving 72.3 mg of spiro-OMeTAD (Lumtec) in 1mL chlorobenzene (SigmaAldrich) and then adding 17.5 μL of 520 mg/mL LiTFSI dopant (Sigma-Aldrich) in acetonitrile (Sigma-Aldrich) and 28.8 μL of tert-butylpyridine (Sigma Aldrich) before filtering through a 0.2 μm PTFE filter. For each device, 40 μL of spiro-OMeTAD solution was spun at 3000rpm for 30 seconds. For organic ETLs in P-I-N, 40 nm C_{60} (MER Corporation) at 0.3 Å s^{-1} followed by 7.5 nm BCP (TCI) at 0.2 Å s^{-1} was thermally evaporated (Angstrom Amod). Finally, 150nm of metal electrode (Kurt J. Lesker) was thermally evaporated through a patterned shadow mask (Ag for organic ETL; Al for TiO_x ETL).

Device Characterization

The perovskite solar cell current−voltage measurements were measured in ambient conditions (45% RH, 25°C) under 1 sun, AM 1.5G illumination performed using a Keithley model 2400 digital source meter and 300W xenon lamp (Oriel) solar simulator. The lamp was calibrated with an NREL-calibrated KG5 filtered Si reference cell. *J−V* curves were taken over an active area of 0.21 cm^2 from forward (1.2V) to reverse bias (-0.05V) sampled at 0.01 V intervals with a 0.1 s delay time at each voltage step before taking data. Maximum power point tracking was performed every 2 s using a perturb and measure software with a voltage step of 0.05 V to continuously track power output.

Film Characterization

X-ray Photoelectron Spectroscopy (XPS) (PHI 5000 Versaprobe, Physical Electronics Inc., US) using an Al−K_{α} (1486 eV) X-ray source operated at 150W was employed for characterizing the chemical compositions of the films. The pass energy was fixed at 117.4 eV for survey scans over a range of 0-1000eV (energy step of 1eV and a time of 20ms) for 5 cycles with a spot size of 200μm^2. An argon ion gun pre-sputter was applied to remove any surface atmospheric contaminants.

X-ray diffraction (XRD) patterns were measured on an X'PERT PRO diffraction system (PANanalytic) equipped with Cu-Kα radiation (λ = 1.5406 Å). Grazing incidence 2θ scans were obtained using a 0.27° parallel plate collimator, a step size of 0.05°, ω = 3.6°, and a dwell time of 1 s for $20° < 2\theta < 60°$ for TiO_x films. 2θ-ω scans in Bragg-Brentano geometry were obtained using a 0.27° parallel plate collimator, a step size of 0.05°, and a dwell time of 1 s for $10° < 2\theta < 70°$ for perovskite films. A baseline correction was applied to remove the broad feature associated with the glass substrate.

Scanning Electron Microscopy (SEM) images were taken with an FEI Magellan 400 XHR (Thermo Fisher Scientific). Samples were coated with 5nm of Au/Pd (60:40) ratio before imaging to mitigate charging. UV-Vis Absorption Spectroscopy was obtained using a spectrophotometer (Agilent Cary 6000i). Roughness measurements were obtained with Atomic Force Microscopy (AFM) (Park NX-10) using a NSC15: Al tip operated in tapping mode. Contact Stylus Profilometry (Veeco Dektak 150) was used to measure the film thickness with a film edge created by masking off a section of the substrate before film deposition. Steady-state photoluminescence and time-resolved photoluminescence were measured using a Horiba FluoroLog Fluorimeter. Test device architectures of glass/perovskite/TiO_x were excited with a 635nm laser (Picoquant P-C-635M and PDL 800-B operating at 2.5 MHz and 8 x 10^{-5} Watts/cm^2 average intensity). A Time-Correlated Single Photon Counting (TCSPC) method was used for lifetime measurements.

Mechanical G_c Testing

TiO_x films were deposited with OA-CVD on an undoped silicon beam, followed by evaporation of 5nm of titanium and 100nm of Al as additional bonding layers. The stack was then bonded to another silicon beam with a brittle room-temperature cured epoxy adhesive (E-20NS) and clamped together to cure overnight. Double cantilever beam (DCB) specimens were loaded under displacement control in a thin-film cohesion testing system (Delaminator DTS, Menlo Park, CA) from which a load, *P*, versus displacement, *Δ*, curve was recorded. Prior to testing, a razor blade is inserted between the silicon beams to initiate a pre-crack. The fracture energy, G_c (J m^{-2}), was measured in terms of the critical value of the applied strain energy release rate, *G*. G_c can be expressed in terms of the critical load, P_c, at which crack growth occurs, the crack length, *a*, the plain strain elastic modulus, E' , of the substrates, and the specimen dimensions : width, *b*, and half-thickness, *h*. G_c is calculated from[58]

$$G_c = \frac{12P_c^2a^2}{b^2E'h^3}\left(1 + 0.64\frac{h}{a}\right)^2 \qquad (1)$$

An estimate of the crack length was experimentally determined from a measurement of the elastic compliance, *dΔ /dP*, using the compliance relationship:

$$a = \left(\frac{d\Delta}{dP} \times \frac{bE'h^3}{8}\right)^{1/3} - 0.64 \times h \qquad (2)$$

All G_c testing was carried out in laboratory air environment (45%RH 25°C). The specimen was loaded in tension with a displacement rate of 1.0μm/s until reaching P_c and then unloaded slightly to determine the compliance before re-loading. This procedure was continued until crack length equaled $L - 4h$, where *L* is the length of the substrate

Conflicts of interest

There are no conflicts to declare.

Acknowledgements

This work was supported by the U.S. Department of Energy's Office of Energy Efficiency and Renewable Energy (EERE) under Solar Energy Technologies Office (SETO) Agreement Number DE-EE0008559. Part of this work was performed at the Stanford Nano Shared Facilities (SNSF), supported by the National Science Foundation under award ECCS-1542152. Additional support was provided by the National Science Foundation Graduate Research Fellowship, awarded to J. Chen and N. Rolston under award DGE-1656518. The authors recognize W. Scheideler, J. Zhang, Y. Ding, O. Zhao, A. Flick, and Z. Pan for their fruitful discussions.

References

1 A. Kojima, K. Teshima, Y. Shirai and T. Miyasaka, *J. Am. Chem. Soc.*, 2009, **131**, 6050–6051.

2 Best Research-Cell Efficiency Chart | Photovoltaic Research | NREL, https://www.nrel.gov/pv/cell-efficiency.html, (accessed 16 February 2020).

3 O. Malinkiewicz, A. Yella, Y. H. Lee, G. M. Espallargas, M. Graetzel, M. K. Nazeeruddin and H. J. Bolink, *Nat. Photonics*, 2014, **8**, 128–132.

4 J. Jeng, Y. Chiang, M. Lee, S. Peng, T. Guo, P. Chen and T. Wen, *Adv. Mater.*, 2013, **25**, 3727–3732.

5 O. Malinkiewicz, C. Roldán-Carmona, A. Soriano, E. Bandiello, L. Camacho, M. K. Nazeeruddin and H. J. Bolink, *Adv. Energy Mater.*, 2014, **4**, 1400345.

6 P.-W. Liang, C.-Y. Liao, C.-C. Chueh, F. Zuo, S. T. Williams, X.-K. Xin, J. Lin and A. K.-Y. Jen, *Adv. Mater.*, 2014, **26**, 3748–3754.

7 V. A. Online, S. Sun, T. Salim, N. Mathews, M. Duchamp, C. Boothroyd, G. Xing, T. C. Sum and Y. M. Lam, *Energy Environ. Sci.*, 2014, **7**, 399–407.

8 Z. Song, C. L. McElvany, A. B. Phillips, I. Celik, P. W. Krantz, S. C. Watthage, G. K. Liyanage, D. Apul and M. J. Heben, *Energy Environ. Sci.*, 2017, **10**, 1297–1305.

9 P. M. Hangoma, Y. Ma, I. Shin, Y. Liu, W. I. Park, Y. K. Jung, B. R. Lee, J. H. Jeong, S. H. Park and K. H. Kim, *Sol. RRL*, 2019, **3**, 1800289.

10 Y. Bai, Q. Dong, Y. Shao, Y. Deng, Q. Wang, L. Shen, D. Wang, W. Wei and J. Huang, *Nat. Commun.*, 2016, **7**, 12806.

11 J. H. Kim, I. Lee, T. S. Kim, N. Rolston, B. L. Watson and R. H. Dauskardt, *MRS Bull.*, 2017, **42**, 115–123.

12 S. R. Dupont, M. Oliver, F. C. Krebs and R. H. Dauskardt, *Sol. Energy Mater. Sol. Cells*, 2012, **97**, 171–175.

13 N. Rolston, B. L. Watson, C. D. Bailie, M. D. McGehee, J. P. Bastos, R. Gehlhaar, J. E. Kim, D. Vak, A. T. Mallajosyula, G. Gupta, A. D. Mohite and R. H. Dauskardt, *Extrem. Mech. Lett.*, 2016, **9**, 353–358.

14 I. S. Kim, D. H. Cao, D. B. Buchholz, J. D. Emery, O. K. Farha, J. T. Hupp, M. G. Kanatzidis and A. B. F. Martinson, *Nano Lett.*, 2016, **16**, 7786–7790.

15 K. A. Bush, C. D. Bailie, Y. Chen, A. R. Bowring, W. Wang, W. Ma, T. Leijtens, F. Moghadam and M. D. McGehee, *Adv. Mater.*, 2016, **28**, 3937–3943.

16 R. Cheacharoen, N. Rolston, D. Harwood, K. A. Bush, R. H. Dauskardt and M. D. McGehee, *Energy Environ. Sci.*, 2018, **11**, 144–150.

17 W. Chen, Y. Wu, Y. Yue, J. Liu, W. Zhang, X. Yang, H. Chen, E. Bi, I. Ashraful, M. Grätzel and L. Han, *Science (80-.).*, 2015, **350**, 944–948.

18 P. Docampo, J. M. Ball, M. Darwich, G. E. Eperon and H. J. Snaith, *Nat. Commun.*, 2013, **4**, 2761.

19 B. Hailegnaw, G. Adam, H. Heilbrunner, D. H. Apaydin, C. Ulbricht, N. S. Sariciftci and

M. C. Scharber, *RSC Adv.*, 2018, **8**, 24836–24846.

20 J. You, L. Meng, T.-B. Song, T.-F. Guo, Y. (Michael) Yang, W.-H. Chang, Z. Hong, H. Chen, H. Zhou, Q. Chen, Y. Liu, N. De Marco and Y. Yang, *Nat. Nanotechnol.*, 2016, **11**, 75–81.

21 Y.-H. Chiang, C.-K. Shih, A.-S. Sie, M.-H. Li, C.-C. Peng, P.-S. Shen, Y.-P. Wang, T.-F. Guo and P. Chen, *J. Mater. Chem. A*, 2017, **5**, 25485–25493.

22 J. Yang, J. Xu, Q. Zhang, Z. Xue, H. Liu, R. Qin, H. Zhai and M. Yuan, *RSC Adv.*, 2020, **10**, 18608–18613.

23 X. Liu, J. Jiang, F. Wang, Y. Xiao, I. D. Sharp and Y. Li, *ACS Appl. Mater. Interfaces*, 2019, **11**, 46894–46901.

24 J. Prochazka, L. Kavan, M. Zukalova, P. Janda, J. Jirkovsky and Z. Vlckova Zivcova, *J. Mater. Res.*, 2013, **28**, 385–393.

25 P. J. Cameron and L. M. Peter, *J. Phys. Chem. B*, 2003, **107**, 14394–14400.

26 L. Kavan, N. Tétreault, T. Moehl and M. Grätzel, *J. Phys. Chem. C*, 2014, **118**, 16408–16418.

27 E. L. Unger, F. Spadavecchia, K. Nonomura, P. Palmgren, G. Cappelletti, A. Hagfeldt, E. M. J. Johansson and G. Boschloo, *ACS Appl. Mater. Interfaces*, 2012, **4**, 5997–6004.

28 H. Hu, B. Dong, H. Hu, F. Chen, M. Kong, Q. Zhang, T. Luo, L. Zhao, Z. Guo, J. Li, Z. Xu, S. Wang, D. Eder and L. Wan, *ACS Appl. Mater. Interfaces*, 2016, **8**, 17999–18007.

29 A. E. Shalan, S. Narra, T. Oshikiri, K. Ueno, X. Shi, H.-P. Wu, M. M. Elshanawany, E. Wei-Guang Diau and H. Misawa, *Sustain. Energy Fuels*, 2017, **1**, 1533–1540.

30 S. S. Mali, C. K. Hong, A. I. Inamdar, H. Im and S. E. Shim, *Nanoscale*, 2017, **9**,

3095–3104.

31 A. Kogo, S. Iwasaki, M. Ikegami and T. Miyasaka, *Chem. Lett.*, 2017, **46**, 530–532.

32 D. Yang, R. Yang, J. Zhang, Z. Yang, S. Liu and C. Li, *Energy Environ. Sci.*, 2015, **8**, 3208–3214.

33 T. Maruyama and S. Arai, *Sol. Energy Mater. Sol. Cells*, 1992, **26**, 323–329.

34 S. Patra, C. Andriamiadamanana, M. Tulodziecki, C. Davoisne, P.-L. Taberna and F. Sauvage, *Sci. Rep.*, 2016, **6**, 21588.

35 B. J. Blackburn, C. Drosos, D. B. Brett, M. A. Parkes, C. J. Carmalt and I. P. Parkin, *RSC Adv.*, 2016, **6**, 111797–111805.

36 C. C. Boyd, R. Cheacharoen, T. Leijtens and M. D. McGehee, *Chem. Rev.*, 2019, **119**, 3418–3451.

37 F. Hilt, M. Q. Hovish, N. Rolston, K. Brüning, C. J. Tassone and R. H. Dauskardt, *Energy Environ. Sci.*, 2018, **11**, 2102–2113.

38 W. J. Scheideler, N. Rolston, O. Zhao, J. Zhang and R. H. Dauskardt, *Adv. Energy Mater.*, 2019, **9**, 1803600.

39 G. E. Eperon, T. Leijtens, K. A. Bush, R. Prasanna, T. Green, J. T.-W. Wang, D. P. McMeekin, G. Volonakis, R. L. Milot, R. May, A. Palmstrom, D. J. Slotcavage, R. A. Belisle, J. B. Patel, E. S. Parrott, R. J. Sutton, W. Ma, F. Moghadam, B. Conings, A. Babayigit, H.-G. Boyen, S. Bent, F. Giustino, L. M. Herz, M. B. Johnston, M. D. McGehee and H. J. Snaith, *Science*, 2016, **354**, 861–865.

40 M. M. Tavakoli, H. T. Dastjerdi, D. Prochowicz, P. Yadav, R. Tavakoli, M. Saliba and Z. Fan, *J. Mater. Chem. A*, 2019, **7**, 14753–14760.

41 K. A. Bush, K. Frohna, R. Prasanna, R. E. Beal, T. Leijtens, S. A. Swifter and M. D. McGehee, *ACS Energy Lett.*, 2018, **3**, 428–435.

42 Y. Li, R. L. Z. Hoye, H. H. Gao, L. Yan, X. Zhang, Y. Zhou, J. L. MacManus-Driscoll and J. Gan, *ACS Appl. Mater. Interfaces*, 2020, **12**, 7135–7143.

43 S. N. Habisreutinger, N. K. Noel and H. J. Snaith, *ACS Energy Lett.*, 2018, **3**, 2472–2476.

44 B. Chen, M. Yang, S. Priya and K. Zhu, *J. Phys. Chem. Lett.*, 2016, **7**, 905–917.

45 W. Tress, *J. Phys. Chem. Lett*, 2017, **8**, 3106–3114.

46 X. Ling, J. Yuan, D. Liu, Y. Wang, Y. Zhang, S. Chen, H. Wu, F. Jin, F. Wu, G. Shi, X. Tang, J. Zheng, S. Liu, Z. Liu and W. Ma, *ACS Appl. Mater. Interfaces*, 2017, **9**, 23181–23188.

47 T. Leijtens, G. E. Eperon, S. Pathak, A. Abate, M. M. Lee and H. J. Snaith, *Nat. Commun.*, 2013, **4**, 2885.

48 W. Li, W. Zhang, S. Van Reenen, R. J. Sutton, J. Fan, A. A. Haghighirad, M. B. Johnston, L. Wang and H. J. Snaith, *Energy Environ. Sci.*, 2016, **9**, 490–498.

49 N. Ahn, K. Kwak, M. S. Jang, H. Yoon, B. Y. Lee, J.-K. Lee, P. V. Pikhitsa, J. Byun and M. Choi, *Nat. Commun.*, 2016, **7**, 13422.

50 R. Liu, L. Wang, Y. Fan, Z. Li and S. Pang, *RSC Adv.*, 2020, **10**, 11551–11556.

51 G. Dubois, W. Volksen, T. Magbitang, R. D. Miller, D. M. Gage and R. H. Dauskardt, *Adv. Mater.*, 2007, **19**, 3989–3994.

52 B. Roose, J.-P. C. Baena, K. C. Gödel, M. Graetzel, A. Hagfeldt, U. Steiner and A. Abate, *Nano Energy*, 2016, **30**, 517–522.

53 Q. Jiang, L. Zhang, H. Wang, X. Yang, J. Meng, H. Liu, Z. Yin, J. Wu, X. Zhang and J. You, *Nat. Energy*, 2017, **2**, 16177.

54 Z. Zhu, Y. Bai, X. Liu, C.-C. Chueh, S. Yang and A. K.-Y. Jen, *Adv. Mater.*, 2016, **28**, 6478–6484.

55 X. Liu, T. Bu, J. Li, J. He, T. Li, J. Zhang, W. Li, Z. Ku, Y. Peng, F. Huang, Y.-B. Cheng and J. Zhong, *Nano Energy*, 2018, **44**, 34–42.

56 Q. Jiang, X. Zhang and J. You, *Small*, 2018, **14**, 1801154.

57 J. P. Correa Baena, L. Steier, W. Tress, M. Saliba, S. Neutzner, T. Matsui, F. Giordano, T. J. Jacobsson, A. R. Srimath Kandada, S. M. Zakeeruddin, A. Petrozza, A. Abate, M. K. Nazeeruddin, M. Grätzel and A. Hagfeldt, *Energy Environ. Sci.*, 2015, **8**, 2928–2934.

58 M. F. Kanninen, *Int. J. Fract.*, 1973, **9**, 83–92.

Figures

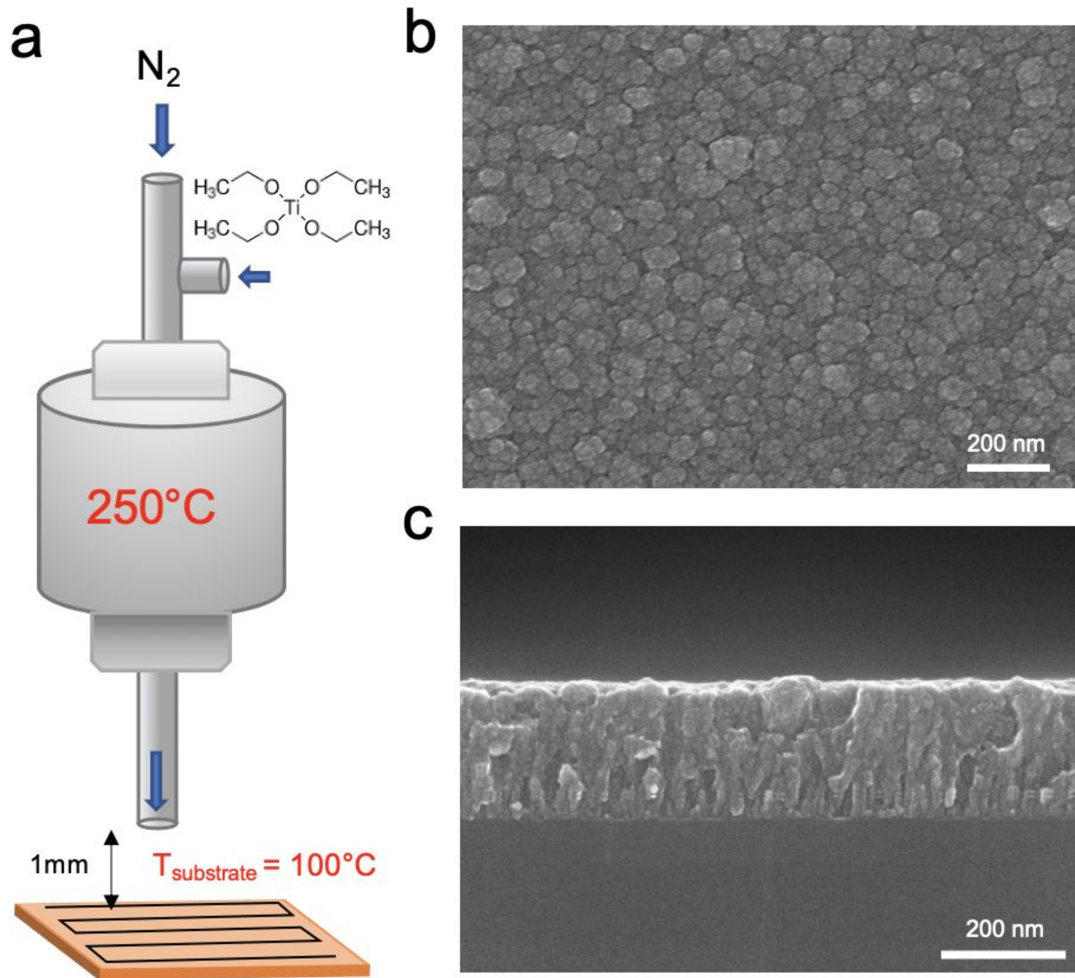

Figure 1: **(a)** OA-CVD setup with titanium ethoxide precursor, flash evaporator, and deposition raster pattern. **(b)** Top down SEM of TiO_x film and **(c)** X-section SEM of ~ 250nm thick TiO_x film.

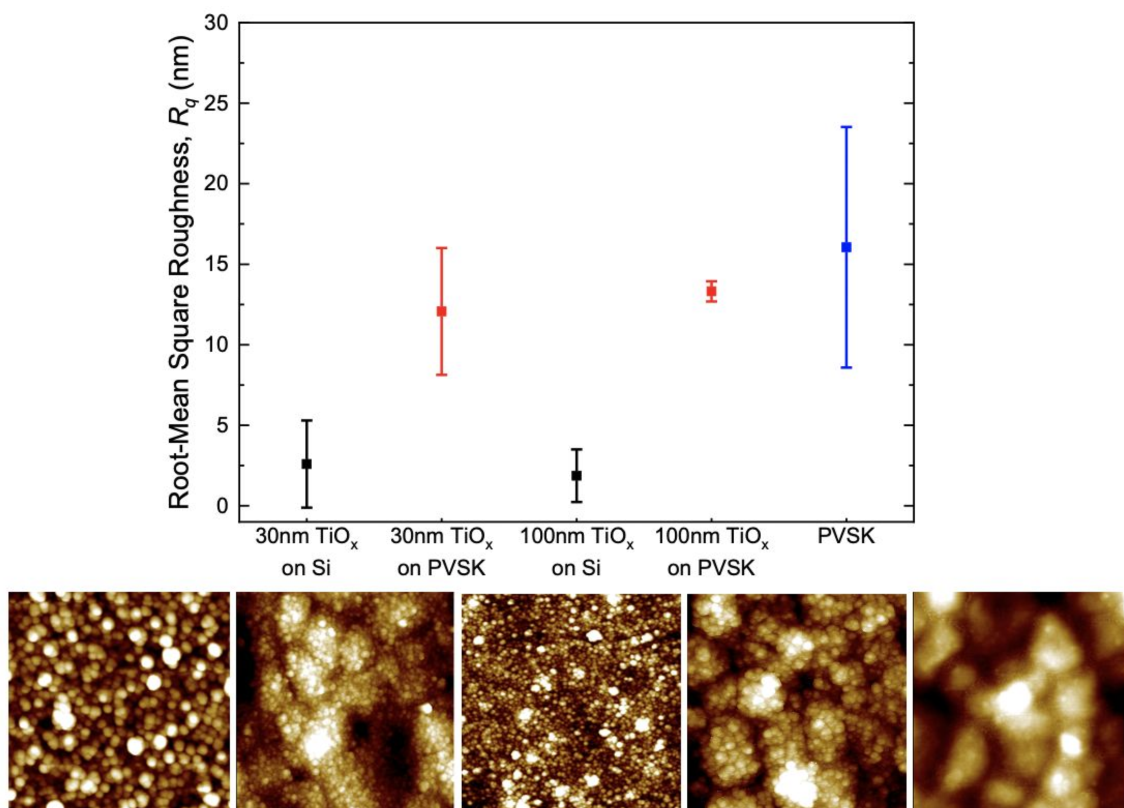

Figure 2: Root-mean-square roughness of 30nm and 100nm thick TiO_x film on silicon or perovskite, and perovskite reference with AFM images of selected films on 1μm^2 area (images are left to right with axis).

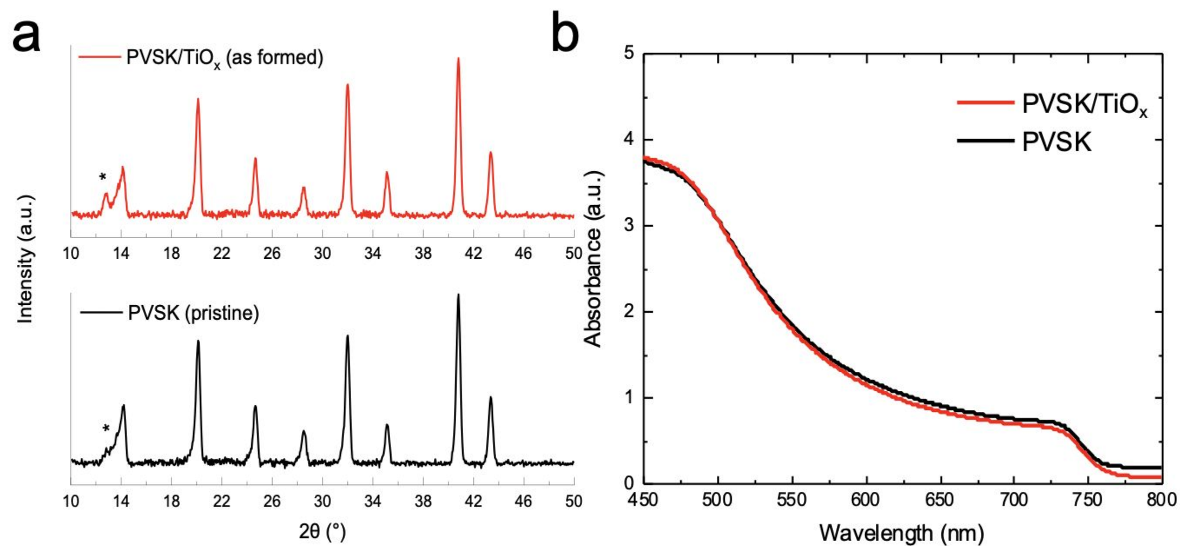

Figure 3: (a) XRD spectra of glass/perovskite (PVSK) test structure before and after TiO_x deposition. PbI_2 peaks are denoted with *. **(b)** UV-Vis absorption spectra before and after TiO_x deposition.

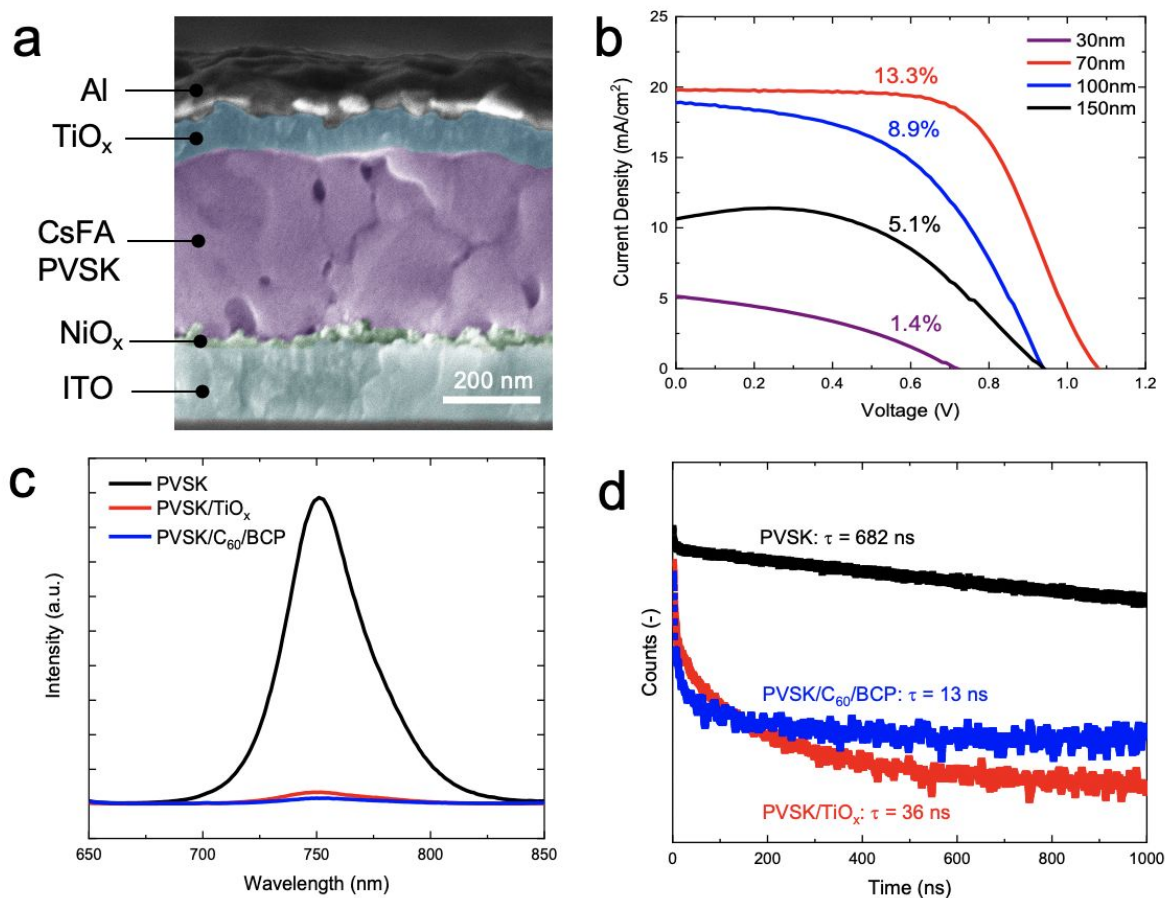

Figure 4: **(a)** Inverted P-I-N device with TiO_x ETL architecture and X-section SEM of fabricated device. **(b)** Device performance with different TiO_x ETL film thickness. **(c)** Steady-state photoluminescence of PVSK and ETLs on glass with **(d)** time-resolved photoluminescence for carrier lifetimes.

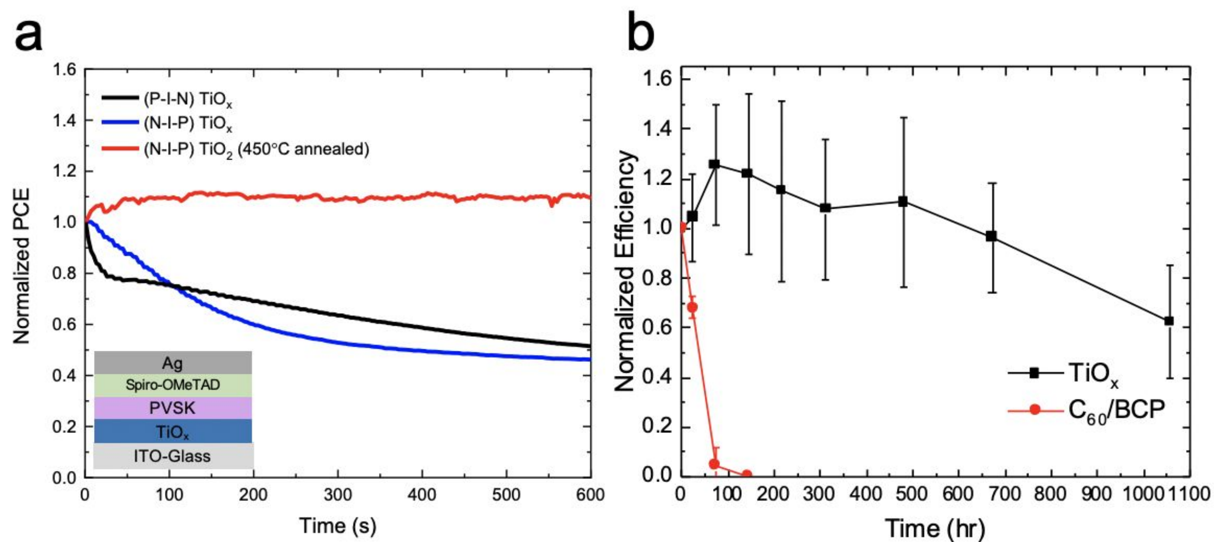

Figure 5: **(a)** Maximum Power Point Tracking (MPPT) of amorphous P-I-N TiO_x devices and crystalline N-I-P TiO_2 devices (inset) **(b)** Normalized efficiency of devices with TiO_x ETL and C_{60}/BCP ETL shelf-aged in uncovered and ambient conditions (25°C, 45% RH) over 1000hr, taken from eight devices over four substrates for each ETL.

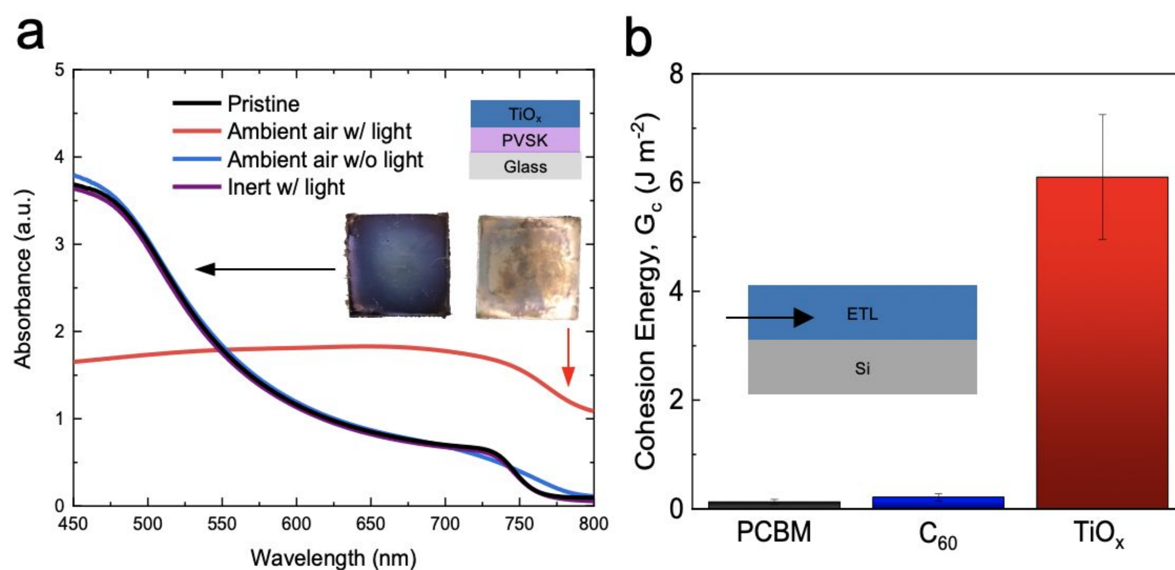

Figure 6: **(a)** UV-Vis absorption spectra of glass/PVSK/TiO_x before and after aging under different conditions for 24 hrs at 40°C (illumination through glass side), with optical images showing degradation. **(b)** G_c ETL comparison of PCBM (spin-coated), C_{60} (thermal evaporation), and TiO_x (OA-CVD) and cohesive fracture path.

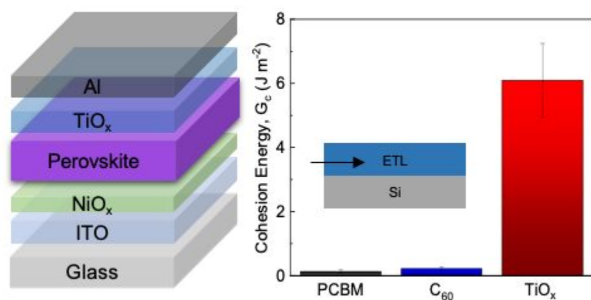

Low-temperature TiO_x electron transport layer (ETL) with improved fracture energy and barrier properties to environmental species compared to organic ETLs.